https://doi.org/10.5194/egusphere-2026-2442
Preprint. Discussion started: 26 May 2026

Quantitative Analysis of the Effect of Flow Velocity on the Size Exclusion Transport of Colloids in Saturated Porous Media

Changxi Wang [a], Zhaofei Duan [a], Xinlin Li[a], Ziyu Zhou[a], Jirka Šimůnek [c], Renkuan Liao [a, b] *

a College of Land Science and Technology, Key Laboratory of Arable Land Conservation in North China, Ministry of Agriculture and Rural Affairs, China Agricultural University, Beijing 100193, P. R. China

b State Key Laboratory of Efficient Utilization of Agricultural Water Resources, China Agricultural University, Beijing 100083, P. R. China.

c Department of Environmental Sciences, University of California Riverside, Riverside, CA 92521, United States.

Corresponding author: Renkuan Liao (renkuanliao@163.com or renkuanliao@cau.edu.cn)

Abstract

Despite extensive studies on colloid transport in porous media, the influence of flow velocity on the size exclusion effect (SEE) remains poorly understood. In this study, nuclear magnetic resonance (NMR) and micro-computed tomography (μ-CT) were employed to characterize the pore structures, and column experiments combined with HYDRUS-1D modeling were conducted to quantitatively analyze colloid transport under varying flow velocities. NMR and μ-CT results indicated that coarser sand possesses a larger average pore diameter. Colloids consistently broke through earlier than the conservative tracer, confirming SEE. Both the relative breakthrough time difference (ΔT_b) and the relative peak arrival time difference (ΔT_peak) decreased with increasing flow velocity, indicating that SEE weakened as flow increased. Across all media, the size exclusion coefficient γ, representing the fraction of water-saturated pore space inaccessible to mobile colloids, decreased from about 0.09–0.14 at low velocity (~0.004 cm s^{-1}) to about 0.03–0.04 at high velocity (~0.03 cm s^{-1}). In addition, γ was generally higher in 10 cm columns than in 30 cm columns, especially at low velocity. Flow simulations further suggested that increasing velocity reduced the dominance of low-velocity regions and enhanced the continuity of active flow pathways. These results indicate that γ is not a fixed geometric constant, but a flow-dependent effective parameter governed by pore accessibility and transport conditions.

Keywords: Size exclusion effect, colloids transport, porosity, NMR, μ-CT

1 Introduction

Colloid transport in porous media is a complex yet critical phenomenon, particularly in environmental contexts such as groundwater contamination, where it strongly influences pollutant fate (Akbulut and Min, 2025; Akdogan and Guven, 2019; Bradford et al., 2013). A key mechanism underlying this process is that colloids are often transported faster than dissolved tracers, a phenomenon attributed to the size exclusion effect (SEE). SEE arises because colloids, owing to their finite dimensions, are unable to access the entire pore volume available to solutes or water molecules (Donath et al., 2019).

Quantitative characterization of pore structures provides a critical basis for evaluating SEE. The occurrence and strength of SEE are primarily governed by the geometry of pore spaces and the relative size of colloids to pore throats (Auset and Keller, 2004; Chakraborty et al., 2024). Micromodel experiments provide direct visual insights into the relationship between colloids and pore-throat sizes at a microscopic scale. For instance, Sirivithayapakorn and Keller (2003) demonstrated that colloids can only enter pore throats larger than ~1.5 times their diameter. At the column scale, however, recent studies have revealed a significant negative linear correlation between the fraction of the water-saturated pore volume inaccessible to mobile colloids (γ) and the median grain size of the porous medium (d_{50}) (Wang et al., 2024). While this correlation suggests a link between the bulk properties of the medium and the extent of SEE, it is an indirect relationship based on the average properties of the entire medium rather than the pores.

Noninvasive techniques such as nuclear magnetic resonance (NMR) and micro-computed tomography (μ-CT) have become mainstream tools for pore structure characterization (Shen et al., 2025; Xiao et al., 2016; Zhao et al., 2017). NMR infers pore size distributions and fluid dynamics from relaxation times (T_2 or T_1–T_2) (Morales-Chávez et al., 2025). It is particularly well-suited for nanoscale characterization, though calibration is required to account for surface relaxation effects. In contrast, μ-CT yields high-resolution 3D images of pore geometry and connectivity at the micrometer scale. However, it typically cannot resolve sub-micron pores (Adhikari et al., 2016). The integration of NMR and μ-CT has emerged as a powerful approach, as the two methods complement each other to provide a multi-scale, high-precision understanding of the pore network structure. Recent advances include finite-element-based NMR modeling to simulate signals for the accurate pore size distribution analysis, as well as NMR–CT data registration approaches that optimize experimental design to determine surface relaxivity (ρ) and predict permeability across scales (Shen et al., 2025; Xiao et al., 2016; Zhao et al., 2017).

In addition to pore structure, flow velocity exerts a profound influence on SEE. Some studies show that increased flow velocities can mitigate SEE. Bai et al. (2015) found that the early breakthrough of colloids decreased as the flow rate increased in their infiltration experiments. Similarly, Massei et al. (2002) observed that with increasing Darcy velocity, colloids showed reduced early breakthrough, with the effect disappearing at velocities over 0.073 cm s^{-1}. They attributed this to changes in flow partitioning: at higher velocities, a larger fraction of the pore volume becomes accessible to colloids, thereby decreasing their exclusion from the pore space. Goppert and Goldscheider (2008) also reported that the time difference between colloid and tracer breakthrough decreased with increasing velocity, suggesting that higher velocities may redirect flow into smaller pores and fractures, thereby enhancing colloid retention.

Conversely, other studies report the opposite trend, suggesting that increasing flow velocity enhances hydrodynamic torque on colloids, thereby promoting detachment from solid surfaces and reducing deposition. This leads to earlier breakthrough and intensification of SEE. For example, Ahfir et al. (2007) observed that at higher Darcy velocities (0.3483 cm s^{-1}), colloids broke through porous media earlier than conservative tracers, whereas at lower velocities (0.0134 cm s^{-1}), tracers emerged first due to greater colloid deposition. Similar findings were reported by Zhang et al. (2016), who noted that colloids exhibited early breakthrough only when the Darcy velocity exceeded a certain threshold.

To address these gaps in understanding SEE, this study integrates μ-CT, NMR, and HYDRUS-1D modeling to clarify how flow velocity regulates SEE in porous media. μ-CT and NMR were used to characterize pore-size distributions and flow heterogeneity. Column experiments at different velocities, combined with HYDRUS-1D fitting, enabled the quantitative determination of the size exclusion coefficient (γ). This framework establishes a mechanistic link between pore structure, flow conditions, and colloid transport behavior, offering a robust tool for predicting colloid fate in natural systems.

2 Materials and Methods

2.1 Silica colloids and porous media

Silica colloids were used as the model particles in this study, characterized by a particle size of 0.5 μm and a zeta potential of -39.1 mV. The colloid concentration was maintained at 100 mg L^{-1}. To investigate the influence of different pore structures on colloid transport, high-purity quartz sands were used as the porous medium. The sands were sieved into three distinct grades: fine, medium, and coarse. Before use, the quartz

https://doi.org/10.5194/egusphere-2026-2442
Preprint. Discussion started: 26 May 2026

sands were thoroughly cleaned to remove organic and iron impurities and minimize colloid deposition. The sands were first soaked in a 2 mol L^{-1} HCl solution at 90°C for 24 h (Wang et al., 2025; Yan et al., 2019). After acid treatment, they were rinsed multiple times with deionized (DI) water to remove residual fines and acid, followed by drying in an oven at 105°C (Yan et al., 2019).

2.2 Column transport experiments

The transport experiments were conducted in a vertical, upward-flow configuration using polymethyl methacrylate (PMMA) columns (2.5 cm diameter; 10 cm or 30 cm length). A peristaltic pump controlled the flow rate from the bottom of the column. The sand was packed into the column under saturated conditions, supported by a nylon membrane to prevent media displacement. The porosity of the packed columns was approximately 0.434. To investigate the effect of flow velocity on colloid transport, experiments were performed at flow rates of 10, 8, 6, 4, 2, and 1 ml min^{-1}. Before each colloid transport experiment and following any change in the flow rate, a conservative tracer ($NaNO_3$) test was performed to characterize the hydrodynamic conditions. The procedure began by equilibrating the column with 5 pore volumes (PVs) of deionized (DI) water. This was followed by an injection of a 0.14 PV pulse of 3 mmol L^{-1} $NaNO_3$. The experiment concluded with a final rinse using 5 PVs of DI water. Throughout the procedure, the effluent concentration of $NaNO_3$ was monitored in real-time at a wavelength of 235 nm using a UV spectrophotometer (TU-1900, Yoke, China).

The silica colloid transport experiments were similar to those used for conservative tracers. After an initial flush with 5 PVs of DI water, a pulse of 0.14 PVs of the silica particle suspension was introduced. This was followed by a final rinse with 5 PVs of

https://doi.org/10.5194/egusphere-2026-2442
Preprint. Discussion started: 26 May 2026

colloid-free DI water to remove unattached particles. The effluent concentrations of silica colloids were quantified in real-time at a wavelength of 300 nm using the same UV spectrophotometer.

2.3 Pore structure characteristic

The intricate pore structure of the quartz sand columns was comprehensively characterized using two complementary noninvasive techniques: Nuclear magnetic resonance (NMR) and X-ray micro-computed tomography (μ-CT). The experimental workflow involved first performing NMR analysis on the fully saturated columns, followed by oven-drying the samples for subsequent μ-CT scanning.

2.3.1 NMR analysis

A standard 2.0 MHz NMR analyzer (LIME-MRI-D12, Beijing Limecho Technology Co., Ltd.) equipped with a 1.5-inch probe was used to determine the pore size distribution (PSD) and porosity of the saturated porous media. A Carr-Purcell-Meiboom-Gill (CPMG) pulse sequence was employed to measure the transverse relaxation time (T_2). The T_2 relaxation of water in the porous media is primarily governed by surface relaxation, which is directly proportional to the pore's surface-to-volume ratio. This physical principle enables a direct correlation between shorter T_2 values and smaller pores, and longer T_2 values with larger pores.

The acquired T_2 decay data are then processed to obtain a T_2 distribution spectrum. This is typically done through an inverse Laplace transform algorithm, which deconvolutes the multi-exponential decay signal into a continuous distribution of relaxation times. Each peak in this T_2 distribution corresponds to a population of pores with a characteristic size.

To convert the T_2 distribution into PSD, a conversion factor (C) is applied, based on the relationship: $r = C^*T_2$, where r is the pore radius. The parameter C is often determined by calibrating with samples of known pore sizes or through independent measurements (e.g., µ-CT).

2.3.2 µ-CT scanning and analysis

µ-CT was utilized to generate a detailed three-dimensional reconstruction of the pore network. A SkyScan 1273 (Bruker, Belgium) was used to scan the samples. To balance high resolution with the sample size, the 10 cm columns were scanned at a resolution of 11 µm. The X-ray source was operated at 125 kV and 64 µA.

The image analysis workflow was initiated by importing the raw CT slices into ImageJ. The grayscale images were then converted to binary representations using an automated thresholding protocol, effectively segmenting the pore space from the solid sand grains. Following binarization, a noise-reduction filter was applied to remove imaging artifacts before a region of interest (ROI) was cropped to focus the analysis on the central portion of the sample. To further characterize the pore network, these binary slices were imported into the Avizo software, which was used to generate a detailed 3D reconstruction (**Figure 1**).

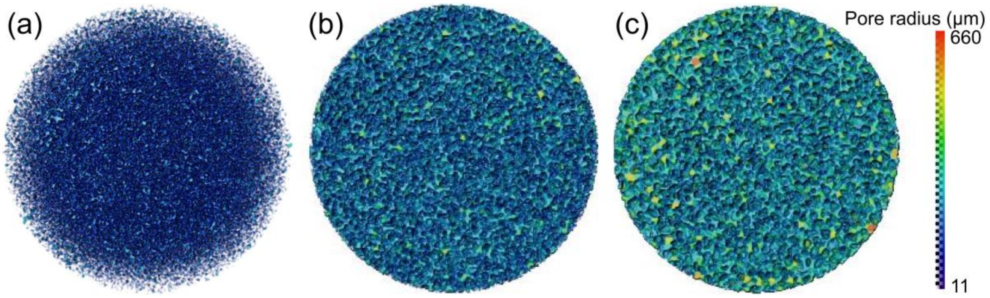

Figure 1. 3D pore structure images of columns filled with three different sands. (a) fine sand, (b) medium sand, and (c) coarse sand. Colors represent relative pore radii: blue corresponds to a narrow pore radius, while red corresponds to a wider pore radius.

To simulate the velocity field within the pore space based on the binarized CT images, a representative pore region was selected from the CT-derived longitudinal section at the middle of the sand column. The selected region had a size of 300 μm in width and 100 μm in height and was used to represent the local spatial distribution of pore channels and grain skeletons in the porous medium. Based on the CT image segmentation results, solid grains and flow-accessible pore spaces were distinguished, and the pore space was extracted as a two-dimensional computational domain. A 2D finite-element model of the pore geometry was developed using COMSOL (version 6.3, Burlington, MA, USA). The incompressible Navier-Stokes equations were solved under steady-state conditions with a triangular mesh to compute relative water velocities and streamlines surrounding the grains (Sirivithayapakorn and Keller, 2003). Boundary conditions comprised no-flow walls along the lateral edges orthogonal to the flow and a uniform pressure gradient between the inlet and outlet.

2.4. Modeling

Colloid transport through saturated sand columns was simulated using HYDRUS-1D, based on a one-dimensional convection–dispersion equation (CDE) considering irreversible attachment and size exclusion (Bradford et al., 2003; Šimůnek et al., 2024). Under steady saturated flow, the transport of a conservative tracer is described as:

$$\frac{\partial \theta C}{\partial t} = -U\frac{\partial C}{\partial x} + \theta D_L \frac{\partial^2 C}{\partial x^2} \tag{1}$$

where C is the tracer concentration (mg L^{-1}), t is time (s), and x is the spatial position (cm). θ is the porosity (cm^3 cm^{-3}), U is the Darcy flux (cm s^{-1}), and $D_L = \alpha_L\, q_w$ is the hydrodynamic dispersion coefficient (cm^2 s^{-1}). The parameter α_L was obtained by fitting the tracer breakthrough curve. Assuming colloid retention does not alter porous properties, colloid transport follows (Grolimund et al., 1998; Ikni et al., 2013; Kretzschmar et al., 1997):

$$\frac{\partial \theta C}{\partial t} = -q_w \frac{\partial C}{\partial x} + \theta D_L \frac{\partial^2 C}{\partial x^2} - \rho \frac{\partial S}{\partial t} \quad (2)$$

$$\rho \frac{\partial S}{\partial t} = \theta K_r C \quad (3)$$

where ρ is soil bulk density (g cm^{-3}), K_r is the colloid retention rate (s^{-1}), and S is the solid phase colloid concentration (mg g^{-1}). To account for size exclusion, the accessible porosity for mobile colloids is expressed as (Bradford et al., 2003; Chrysikopoulos and Katzourakis, 2015; Wang et al., 2024):

$$\theta_p = \theta - \gamma\theta \quad (4)$$

where γ represents the fraction of pore space inaccessible to colloids (Bradford et al., 2003; Wang et al., 2025; Wang et al., 2024). Substituting Eq. (4) into Eq. (2) yields:

$$\frac{\partial \theta_p C}{\partial t} = -U \frac{\partial C}{\partial x} + \theta_p D_L \frac{\partial^2 C}{\partial x^2} - \theta_p K_r C \quad (5)$$

Eqs. (1)-(5) were numerically solved using HYDRUS-1D, which applies the Levenberg-Marquardt algorithm to invert experimental breakthrough curves (BTCs) and optimize transport parameters (Bradford et al., 2003; Šimůnek et al., 2024).

To compare the relative importance of advective transport and diffusion under different flow velocities and column lengths, the column-scale Peclet number was calculated as (Kretzschmar et al., 1997):

$$Pe_L = \frac{vL}{D_0} \quad (6)$$

https://doi.org/10.5194/egusphere-2026-2442
Preprint. Discussion started: 26 May 2026

where v is the pore-water velocity (cm s^{-1}), calculated from the Darcy velocity U and porosity θ as $v=U/\theta$; L is the column length (cm); and D_0 is the diffusion coefficient of colloidal particles in water (cm^2 s^{-1}). For spherical colloidal particles, D_0 was estimated using the Stokes–Einstein equation:

$$D_0 = \frac{k_B T}{3\pi\mu d_p} \tag{7}$$

where k_B is the Boltzmann constant (J K^{-1}), T is the absolute temperature (K), μ is the dynamic viscosity of water (Pa s), and d_p is the colloid particle diameter (m). The resulting D_0, originally obtained in m^2 s^{-1}, was then converted to cm^2 s^{-1} for the calculation of the Pe_L.

3 Results

3.1 Pore size characterization

Figure 1 visualizes the reconstructed three-dimensional pore-topology structures of the three sand packs from μ-CT scans. The evolution of the color gradient, from deep blue to orange-red, intuitively maps the spatial distribution of pore radii: blue regions indicate narrow flow pathways, whereas red regions represent more open pore spaces. From fine sand (a) to coarse sand (c), the pore space undergoes pronounced geometric reorganization. The fine-sand column (a) exhibits a highly compact and relatively uniform pore network, with the space being almost entirely occupied by narrow flow channels (deep-blue regions). Such extreme spatial confinement would substantially limit colloid transport. In contrast, as the grain size increases, the coarse-sand column (c) contains markedly more large pores (yellow and red patches), resulting in a much broader pore-size distribution range.

Figure 2 shows the volume-weighted pore size distribution (PSD) of the sand columns obtained by μ-CT and the NMR T_2 spectra distributions of the three sand types. The transverse relaxation time T_2 can be converted into an equivalent pore radius, and the signal amplitude is related to the pore volume of water-filled pores. Thus, the distribution of NMR T_2 spectra can reflect the corresponding PSD. As shown in **Figure 2a**, one peak is observed in the PSD curves obtained by μ-CT. However, as shown in **Figure 2b**, the T_2 spectra distributions of the column display two peaks. This discrepancy arises primarily from limitations of μ-CT resolution. For instance, in the study by Peng et al. (2014), lower-resolution images (e.g., 5.92 μm voxel size) fail to detect small pores below that threshold, leading to underestimated porosity and surface area of Berea sandstone. Elkhoury et al. (2019) highlighted that μ-CT voxel sizes of 2-10 μm underestimate porosity in sandstones and limestones by missing sub-resolution pores, affecting quantitative transport calculations. The small peak in the NMR spectrum located between 10^{-2} and 10^{0} ms may be attributed to bound water on the rough surfaces of quartz sand particles, as surface roughness increases the effective surface area and enhances surface relaxation, leading to faster T_2 decay and the emergence of short relaxation components (Keating, 2014).

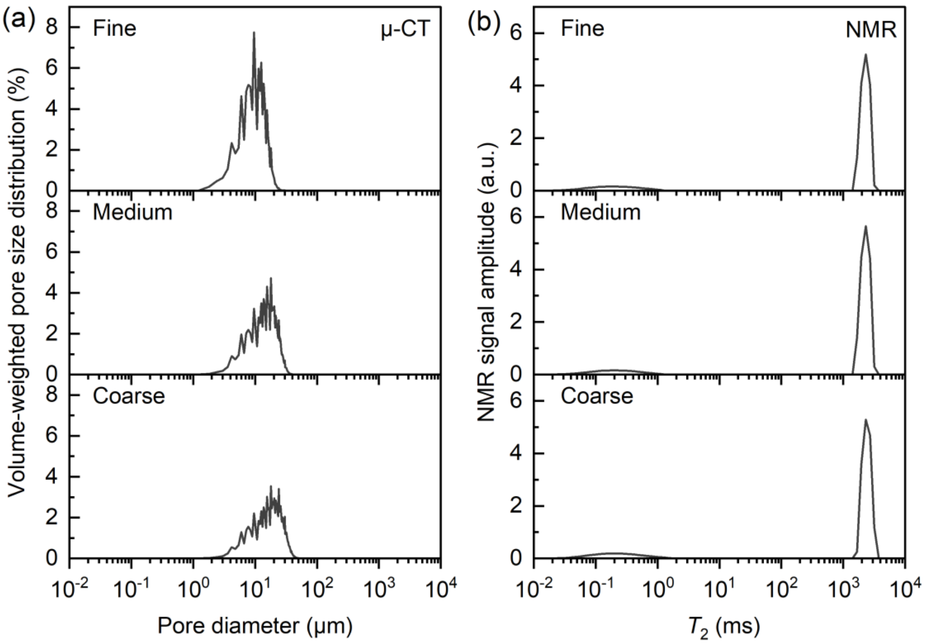

Figure 2. Pore structure characterization of the sand columns using μ-CT and NMR. (a) Volume-weighted pore size distributions (PSD) obtained by μ-CT scanning. (b) NMR transverse relaxation time (T_2) spectra, where the signal amplitude represents the relative contribution of water-filled pores with different relaxation times. Fine sand at the top, medium sand in the middle, and coarse sand at the bottom.

Previous studies have confirmed a correspondence between NMR- and μ-CT-derived PSD curves within intermediate pore-size ranges, often calibrated using equivalent diameter assumptions to account for geometric differences (Zhao et al., 2017). To explore this further, the radius of each pore and the corresponding pore volume obtained by μ-CT were quantified to derive the pore volume distributions of the tested cores. **Figure 3** shows the NMR T_2 spectrum curves and the pore volume distributions obtained by μ-CT for each sample. The peak of the T_2 spectrum curve aligns well with the pore volume distribution obtained by μ-CT for each sample, indicating a reliable correlation in the detectable range. However, this quantitative relationship weakens across the full T_2 spectrum, mainly because X-ray scans can only detect pore sizes larger than half the voxel size (Nagel et al., 2021; Zhao et al., 2017), leading to an underrepresentation of sub-resolution pores. While the PSD measurement range of μ-CT is limited, it remains valuable for validating NMR spectra within overlapping pore-size regimes, thereby enhancing overall characterization of heterogeneous porous media, such as sand columns (Shen et al., 2025; Xiao et al., 2016; Zhao et al., 2017).

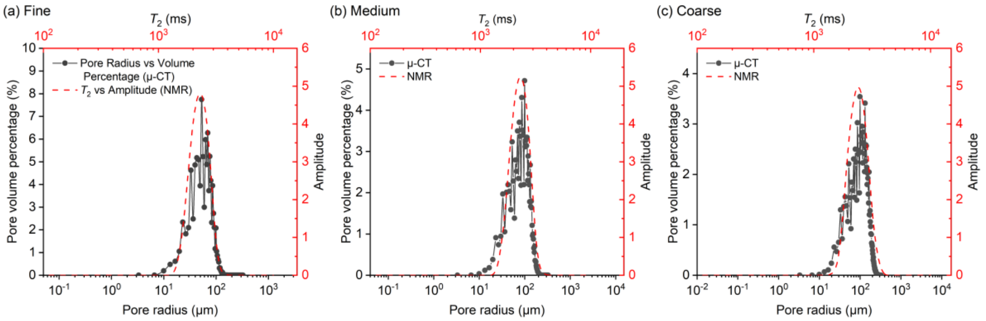

Figure 3. Comparison of the pore size distributions obtained using μ-CT with the distribution of transverse relaxation time T_2 obtained using NMR for the tested artificial cores. (a)-(c) show the results for the fine, medium, and coarse sands, respectively.

Combined μ-CT and NMR analyses revealed distinct pore structural characteristics among the three porous media. The PSDs of the three media types, spanning from the nanometer to micrometer scale, were derived from NMR T_2 relaxation time spectra in conjunction with μ-CT analysis (**Table 1**). The T_2 spectra were converted to PSD using a conversion factor C, calibrated to ensure consistency between the two methods within their overlapping ranges and to mitigate errors arising from microscopic heterogeneity. The conversion factor C was found to increase from the fine to the coarse media (25.0 to 42.9 μm s^{-1}). This trend reflects the need to adjust the surface relaxivity coefficient as the medium coarsens. The bimodal distribution observed in the NMR T_2 spectra was successfully translated into a bimodal PSD, with the two peaks corresponding to pore diameters P_1 and P_2. The diameter associated with the first peak (P_1) increased slightly from 9.0×10^{-3} μm for fine medium to 15.6×10^{-3} μm for coarse medium. Concurrently, the diameter of the second peak (P_2) exhibited a pronounced increase from 115.6 μm to 198.0 μm as the medium became coarser. This trend is a direct consequence of larger interstitial spaces created by coarser particles (Gao et al., 2023).

Table 1. Pore size distribution for three media types, determined using the NMR T_2 relaxation time spectra in conjunction with μ-CT analysis and a conversion factor C.

Media type	Total porosity (θ_{total})	C (μm s^{-1})[a]	P_1 ($\times 10^{-3}$ μm)[b]	P_2 (μm)[c]
Fine	0.434	25.0	9.0	115.6
Medium	0.434	39.9	14.6	184.4
Coarse	0.434	42.9	15.6	198.0

[a] C represents a conversion factor used to transform NMR T_2 relaxation times into pore diameters;
[b] P_1 represents the pore diameter corresponding to the first peak in the NMR PSD;
[c] P_2 represents the pore diameter for the second peak in the NMR PSD.

3.2 Colloid breakthrough curves

Figure 4 presents the observed and fitted breakthrough curves (BTCs) of a conservative tracer ($NaNO_3$) and 0.5 μm silica colloids in sand columns. The columns, 10 cm and 30 cm long, were packed with fine, medium, and coarse quartz sands. The results demonstrate that the peak and shape of the BTCs are strongly dependent on flow velocity. Crucially, the colloids consistently exhibited an earlier breakthrough compared to the conservative tracer. This phenomenon provides compelling evidence of the size exclusion effect (SEE), highlighting the distinct transport kinetics of colloids relative to the solute transport signals.

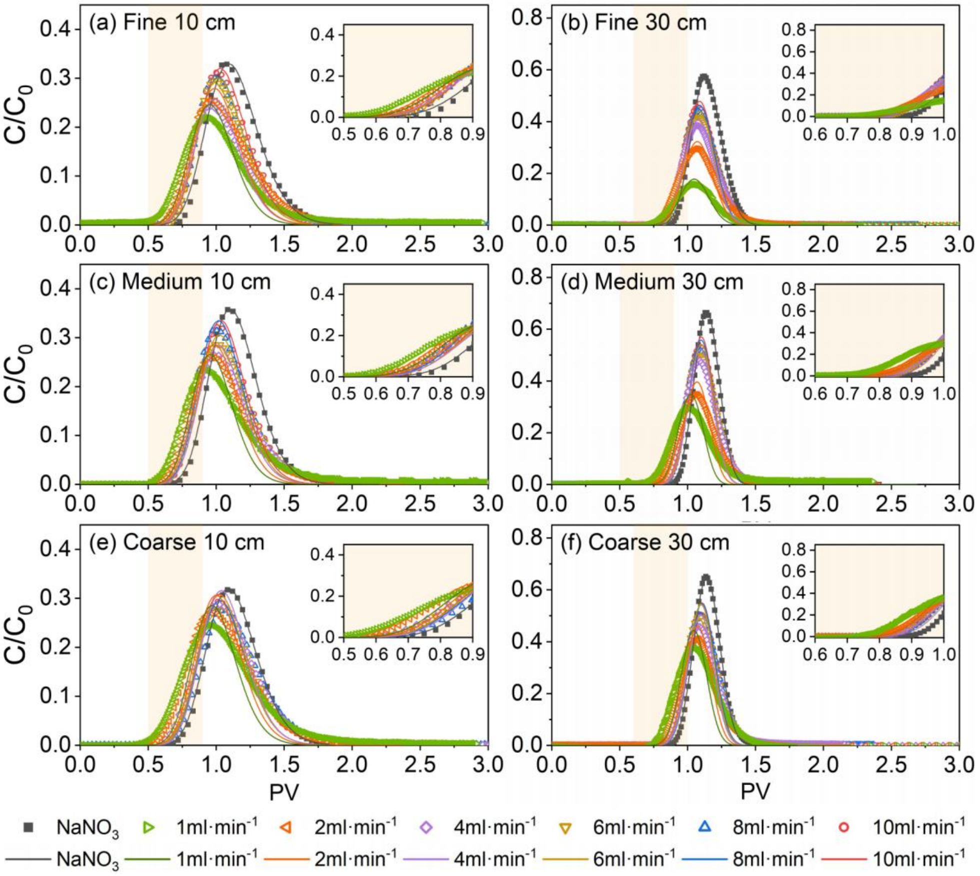

Figure 4. The observed and fitted breakthrough curves of NaNO$_3$ and silica colloids in saturated porous media at different flow rates: in fine sand with column lengths of 10 cm (a) and 30 cm (b), medium sand with column lengths of 10 cm (c) and 30 cm (d), and coarse sand with column lengths of 10 cm (e) and 30 cm (f). A small inset image in the upper right corner of each figure displays a magnified view of the highlighted yellow region.

Additionally, the BTCs of the colloids exhibit a strong dependence on the flow rate. As the flow velocity increases, the BTC peaks for silica colloids become notably sharper, accompanied by a marked increase in the overall recovery rate (**Table 2**). At lower flow rates (1–4 ml min^{-1}), the peak effluent concentrations were low with recoveries ranging from 0.5 to 0.9. In contrast, higher flow rates (6-10 ml min^{-1}) yield elevated recovery, reaching approximately 0.7-1.0. This phenomenon reflects the dual role of flow rate in regulating colloid deposition kinetics. First, higher flow velocities significantly shorten the residence time of colloids within the porous media, reducing the probability of particles contacting and attaching to solid surfaces. Second, increased flow rates strengthen local hydrodynamic shear, which effectively weakens the interaction between colloids and media surfaces, thereby suppressing the tendency for deposition. These results align with established transport principles, where higher velocities typically reduce particle retention and enhance mobility (Ahfir et al., 2007; Benamar et al., 2005). Similarly, Kretzschmar and Sticher (1998) observed stronger breakthrough for latex microspheres at higher flow rates. Torkzaban et al. (2015) further demonstrated that increased shear associated with higher velocities weakens colloid-surface interactions, thereby reducing deposition and promoting particle mobility.

Table 2. Experimental and fitted parameters for colloid transport in three types of porous media under different Darcy velocities.

Media type	Column length (cm)	Flow velocity (ml min^{-1})	Darcy velocity (cm s^{-1})	Dispersity (cm)	Effective porosity (cm^{3}cm^{-3})	γ (-)	Recovery rate (-)
Coarse	30	10.091	0.032	0.091	0.425	0.020	0.937
	30	8.306	0.026	0.091	0.419	0.034	0.946
	30	6.179	0.019	0.091	0.420	0.033	0.942
	30	4.104	0.013	0.091	0.418	0.038	0.906
	30	2.142	0.007	0.091	0.410	0.054	0.790
	30	1.126	0.004	0.091	0.405	0.066	0.728
	10	9.376	0.029	0.147	0.409	0.058	0.990
	10	7.773	0.024	0.147	0.408	0.060	0.956
	10	6.001	0.019	0.147	0.407	0.062	0.946
	10	4.209	0.013	0.147	0.405	0.066	0.914
	10	2.184	0.007	0.147	0.400	0.079	0.828
	10	1.181	0.004	0.147	0.384	0.116	0.826
Medium	30	9.813	0.031	0.080	0.417	0.039	0.929
	30	8.064	0.025	0.080	0.418	0.037	0.888
	30	6.299	0.020	0.080	0.416	0.041	0.823
	30	4.219	0.013	0.080	0.416	0.042	0.832
	30	2.255	0.007	0.080	0.411	0.054	0.627
	30	1.177	0.004	0.080	0.401	0.077	0.645
	10	9.963	0.031	0.135	0.407	0.062	0.955
	10	8.172	0.026	0.135	0.408	0.061	0.944
	10	5.901	0.019	0.135	0.407	0.062	0.909
	10	3.944	0.012	0.135	0.407	0.063	0.892
	10	2.083	0.007	0.135	0.399	0.081	0.804
	10	1.156	0.004	0.135	0.383	0.118	0.741
Fine	30	10.108	0.032	0.127	0.417	0.038	0.877
	30	8.011	0.025	0.127	0.418	0.038	0.806
	30	6.009	0.019	0.127	0.418	0.036	0.737
	30	4.291	0.013	0.127	0.414	0.046	0.547
	30	2.333	0.007	0.127	0.408	0.060	0.547
	30	1.202	0.004	0.127	0.401	0.076	0.549
	10	10.005	0.031	0.156	0.408	0.061	0.947
	10	7.848	0.025	0.156	0.406	0.065	0.927
	10	5.915	0.019	0.156	0.408	0.061	0.902
	10	3.918	0.012	0.156	0.394	0.092	0.820
	10	2.162	0.007	0.156	0.392	0.098	0.814
	10	1.175	0.004	0.156	0.373	0.141	0.700

To further analyze the size exclusion behavior, the relationships between flow velocity and two characteristic parameters of early breakthrough were examined (**Figure 5**). These

https://doi.org/10.5194/egusphere-2026-2442
Preprint. Discussion started: 26 May 2026

parameters were ΔT_b (the relative time difference at C/C_0=0.05) and ΔT_{peak} (the relative time difference at the peak concentration) between colloids of different sizes and a conservative tracer. Larger ΔT values (for both ΔT_b and ΔT_{peak}) indicate more pronounced early breakthrough and a size exclusion effect. The results consistently showed that as flow velocity (U) increased, both ΔT_b and ΔT_{peak} decreased significantly, for all three media and both column lengths.

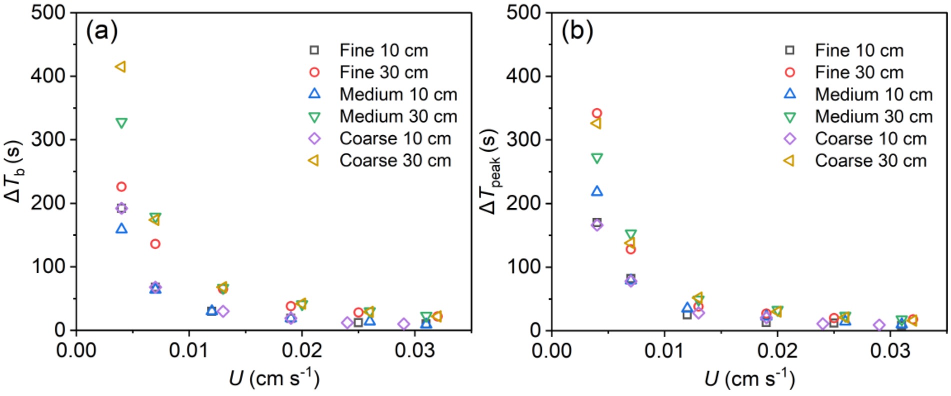

Figure 5. The relationship between the difference in breakthrough times (ΔT_b, a) and peak arrival times (ΔT_{peak}, b) between colloids and a conservative tracer as a function of Darcy velocity (U) in different sand (fine, medium, and coarse) columns of different lengths (10 and 30 cm).

3.3 The size exclusion parameter γ

Given that analyzing the SEE of colloids based on ΔT values provides a relatively macroscopic perspective, Hydrus-1D modeling was employed to quantify SEE using the fitted parameter γ (Bradford et al., 2003; Wang et al., 2025; Wang et al., 2024). In this numerical framework, γ represents the fraction of water saturation that is inaccessible to mobile colloids. The fitted results are presented in **Table 1**, and the relationship between Darcy velocity and γ is shown in **Figure 6**. It is evident that γ exhibits an inverse relationship with flow velocity across all media types and column lengths. The reduction in γ is most pronounced in the low-velocity regime. In particular, for $U < 0.01$ cm s^{-1}, γ exhibits a sharp decline, whereas the rate of decrease becomes progressively smaller at higher velocities, indicating a clear nonlinear sensitivity to flow conditions. For instance, in the 30 cm coarse sand column, γ is only 0.032 at a velocity of 0.032 cm s^{-1}, but it rises to 0.087 when the velocity drops to 0.004 cm s^{-1}. This dynamic behavior of γ is consistent with the previously observed inverse relationship, in which ΔT decreases as flow velocity increases.

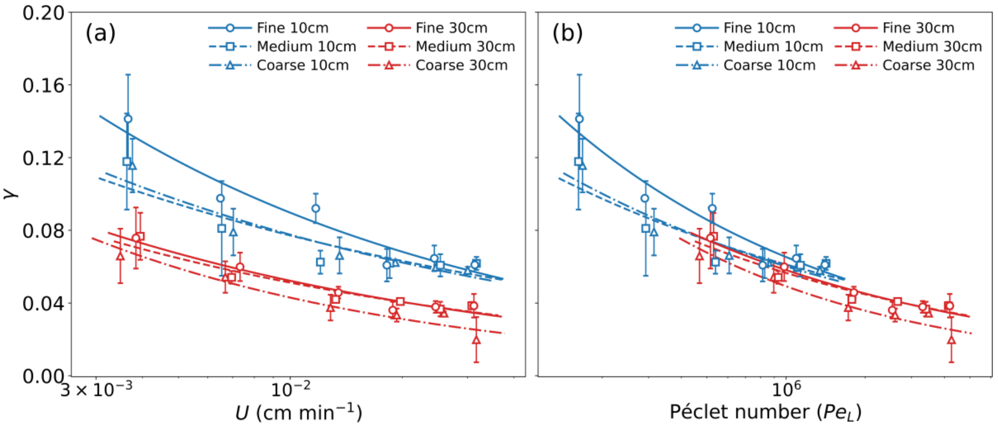

Figure 6. Variation of size exclusion parameter γ with hydrodynamic conditions. (a) the relationship between γ and Darcy velocity (U); (b) the relationship between γ and Péclet number (Pe). Dashed lines represent fitted power-law regressions.

To further evaluate the role of hydrodynamic conditions, γ was also plotted against the Péclet number (Pe) in **Figure 6b**. The same monotonic decrease was observed, showing that the weakening of SEE is associated not only with increasing Darcy velocity, but also with the increasing dominance of advective transport relative to diffusive exchange. This result suggests that γ is not merely a geometric descriptor of pore space, but a dynamic parameter that is strongly modulated by hydrodynamic conditions.

The dashed lines in **Figure 6** represent power-law regressions fitted to the γ–U and γ–Pe relationships, and the corresponding parameters are summarized in **Table 3**. Overall, the regressions provided good fits to the experimental data (R^2 = 0.883–0.997 for γ–U and R^2 = 0.926–0.987 for γ–Pe). Although the fitted coefficient a varied among media and column lengths, the exponent b was consistently negative, confirming the inverse dependence of γ on hydrodynamic forcing. Moreover, the absolute value of b tended to be larger in the coarse sand, particularly for the 30 cm column, implying a stronger sensitivity of γ to flow conditions in more open pore networks.

Table 3. Parameters fitted to the functional relationships between γ and U or Pe.

Media type	Column length (cm)	a (s^b cm^{-b})	b (-)	R^2	Equation
Fine	10	0.017	-0.374	0.964	$\gamma = a \cdot U^b$
Fine	30	0.010	-0.383	0.926	
Medium	10	0.016	-0.392	0.963	
Medium	30	0.007	-0.454	0.949	
Coarse	10	0.015	-0.384	0.967	
Coarse	30	0.005	-0.526	0.987	
Fine	10	15.235	-0.395	0.919	$\gamma = a \cdot Pe^b$
Fine	30	8.707	-0.363	0.927	
Medium	10	3.306	-0.289	0.823	
Medium	30	5.901	-0.336	0.916	
Coarse	10	4.769	-0.317	0.929	
Coarse	30	28.638	-0.461	0.870	

4 Discussions

The apparent dependence of γ on flow velocity, as observed in Table 2 and Figure 6. By definition, γ represents the accessible pore fraction for mobile colloids and, from a purely geometric perspective, should primarily be governed by the size ratio between colloids and pore structures. However, in practice, finite-sized particles do not uniformly sample the entire pore space but instead interact selectively with the pore-scale velocity field. As demonstrated by James and Chrysikopoulos (2003), finite-size colloids are excluded from near-wall low-velocity regions and preferentially travel along faster streamlines, resulting in effective velocities exceeding the mean fluid velocity. Consequently, γ inferred from BTC fitting reflects an effective transport parameter rather than a fixed geometric fraction independent of flow.

The inverse relationship between γ and flow velocity observed in this study is consistent with previous studies reporting that colloid early breakthrough becomes less pronounced as velocity increases. Massei et al. (2002) found that the temporal separation between colloid and solute breakthrough decreased with increasing Darcy velocity, while Bai et al. (2015) similarly reported weaker preferential colloid breakthrough at higher seepage velocities. Goppert and Goldscheider (2008) also showed that the difference between colloid and solute transport diminished under high-flow conditions. These studies collectively support the idea that increasing flow velocity expands the effective flow domain involved in colloid transport, thereby reducing the apparent excluded fraction.

At low flow velocities, the pore-scale velocity field is more strongly partitioned into high-velocity channels and weakly advective or quasi-stagnant regions. Under such conditions, colloids remain concentrated in a limited number of preferential pathways, whereas adjacent low-velocity pore domains are only weakly sampled within the experimental timescale. Pore-scale simulations by Samari Kermani et al. (2020) demonstrated that low-flow conditions favor particle retention and nonuniform transport in constricted and poorly connected pores. Mao et al. (2020) further reported that low velocity enhances localized retention in heterogeneous porous media. In addition, Zhao et al. (2020) showed that lower velocities can prolong colloid residence near collector surfaces, thereby increasing the likelihood of deposition under favorable interfacial conditions.

As flow velocity increases, the pore-scale flow field undergoes systematic reorganization. Enhanced hydraulic gradients at pore throats increase hydrodynamic drag forces, reducing colloid residence in low-velocity zones (Nishad et al., 2021). At the same time, colloid sampling of the velocity field shifts toward sustained transport along connected high-velocity pathways, decreasing the likelihood of entering or remaining in stagnant zones. Pore-scale modeling confirms that increased flow velocity enhances the continuity of active flow paths and reduces localized retention (Samari Kermani et al., 2020). Consequently, flow pathways that are effectively inaccessible under low-flow conditions become increasingly utilized at higher velocities, leading to an increase in effective pore accessibility and a corresponding decrease in γ.

These analyses were further supported by finite element flow simulations (**Figure 7**). At low velocity (0.004 cm s^{-1}), the simulated velocity field exhibited extensive dark-blue zones near pore walls and throats, indicating slow-flow regions. With higher velocity (0.03 cm s^{-1}), the flow field transitioned to light-blue and yellow regions, indicating the activation of smaller pores and the formation of more continuous flow pathways. It should be emphasized, however, that the μ-CT resolution of 11 μm does not allow direct resolution of the sub-micron pores inferred from the NMR T_2 spectra. Thus, the simulations should not be interpreted as direct evidence that colloids entered unresolved micropores at higher velocity. Rather, they provide indirect support for a redistribution of the pore-scale hydraulic field.

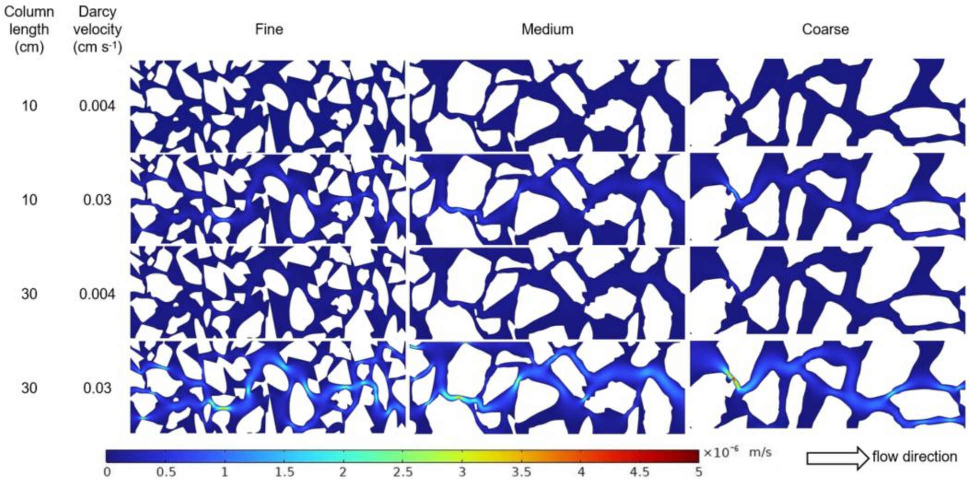

Figure 7. Finite element flow simulations for different column lengths (top to bottom), quartz sand media types (left to right), and Darcy velocities.

5 Conclusions

By integrating NMR, μ-CT, column experiments, and HYDRUS-1D modeling, this study systematically quantified the influence of flow velocity on the size exclusion transport of colloids in saturated porous media. Colloids consistently broke through earlier than the conservative tracer, confirming the occurrence of size exclusion across all tested media. However, the strength of this effect decreased with increasing flow velocity, as demonstrated by both the breakthrough-time metrics and the fitted size exclusion coefficient γ. These results indicate that colloid exclusion is governed not only by pore-size constraints, but also by hydrodynamic regulation of pore-space accessibility.

The fitted γ values showed that γ is best understood as a flow-dependent effective parameter rather than a fixed geometric property. Under low-flow conditions, colloid transport was concentrated in preferential pathways, leading to a larger apparent inaccessible pore fraction; under higher velocities, more of the pore network became hydraulically accessible, resulting in smaller γ values. Column length further modulated this behavior, with shorter columns generally exhibiting stronger apparent exclusion than longer columns. Together, these findings demonstrate that colloid size exclusion reflects the coupled effects of pore structure, flow conditions, and transport distance, and they provide a stronger physical basis for predicting colloid transport in natural and engineered subsurface systems.

Authorship contribution

Changxi Wang: Data curation, Investigation, Methodology, Formal analysis, Visualization, Writing – original draft.

Zhaofei Duan: Investigation, Methodology.

Xinlin Li: Investigation.

Ziyu Zhou: Investigation, Data curation.

Jirka Šimůnek: Supervision, Writing – review & editing.

Renkuan Liao: Conceptualization, Supervision, Resources, Funding acquisition, Writing – review & editing

Conflict of Interest

The authors declare no conflicts of interest relevant to this study.

Data Availability Statement

All data supporting the findings of this study are openly available. The NMR measurements, μ-CT pore-structure data, colloid breakthrough curves, and size exclusion parameters are available at Wang (2025).

Acknowledgment

This work was supported by the National Natural Science Foundation of China (42477317) and Chinese Universities Scientific Fund (15053343).

https://doi.org/10.5194/egusphere-2026-2442
Preprint. Discussion started: 26 May 2026

References

Adhikari, P., Anderson, S.H., Udawatta, R.P. and Kumar, S. 2016. Analysis of CT-measured pore characteristics of porous media relative to physical properties. Procedia Comput. Sci. 95, 442-449.

Ahfir, N.D., Wang, H.Q., Benamar, A., Alem, A., Massei, N. and Dupont, J.P. 2007. Transport and deposition of suspended particles in saturated porous media: Hydrodynamic effect. Hydrogeol. J. 15(4), 659-668.

Akbulut, M.E.S. and Min, Y. 2025. Energy-related contaminants in subterranean waterbodies: The role of geocolloids on facilitated and hindered transport. Next Sustainability 6, 100094.

Akdogan, Z. and Guven, B. 2019. Microplastics in the environment: A critical review of current understanding and identification of future research needs. Environ. Pollut. 254, 113011.

Auset, M. and Keller, A.A. 2004. Pore-scale processes that control dispersion of colloids in saturated porous media. Water Resour. Res. 40(3), W03503.

Bai, B., Zhang, P.Y., Song, X.M., Guo, Z.G. and Chen, X.X. 2015. Transport processes of suspended particles in saturated porous media by column seepage tests. Chin. J. Geotech. Eng. 37(10), 1786-1793.

Benamar, A., Wang, H.Q., Ahfir, N.D., Alem, A., Massei, N. and Dupont, J.P. 2005. Flow velocity effects on the transport and the deposition rate of suspended particles in a saturated porous medium. CR Geosci. 337(5), 497-504.

Bradford, S.A., Morales, V.L., Zhang, W., Harvey, R.W., Packman, A.I., Mohanram, A. and Welty, C. 2013. Transport and fate of microbial pathogens in agricultural settings. Crit. Rev. Environ. Sci. Technol. 43(8), 775-893.

Bradford, S.A., Šimůnek, J., Bettahar, M., van Genuchten, M.T. and Yates, S.R. 2003. Modeling colloid attachment, straining, and exclusion in saturated porous media. Environ. Sci. Technol. 37(10), 2242-2250.

Chakraborty, S., Elhaj, R., Foppen, J.W. and Schijven, J.F. 2024. Dispersion of silica-encapsulated DNA magnetic particles in a homogeneous sand tank. J. Contam. Hydrol. 266, 104410.

Chrysikopoulos, C.V. and Katzourakis, V.E. 2015. Colloid particle size-dependent dispersivity. Water Resour. Res. 51(6), 4668-4683.

Donath, A., Kantzas, A. and Bryant, S. 2019. Opportunities for particles and particle suspensions to experience enhanced transport in porous media: A review. Transp. Porous Media 128(2), 459-509.

Elkhoury, J.E., Shankar, R. and Ramakrishnan, T.S. 2019. Resolution and limitations of X-Ray micro-CT with applications to sandstones and limestones. Transp. Porous Media 129(1), 413-425.

Gao, W., Li, Y., Kong, D., Luan, H., Chen, X., Qi, H. and Tang, X. 2023. Effect of grain size distribution on pore size distribution characteristics in a conglomerate reservoir from an alluvial fan via artificial rock approach. SPE J. 28(06), 3063-3078.

Goppert, N. and Goldscheider, N. 2008. Solute and colloid transport in karst conduits under low- and high-flow conditions. Ground Water 46(1), 61-68.

Grolimund, D., Elimelech, M., Borkovec, M., Barmettler, K., Kretzschmar, R. and Sticher, H. 1998. Transport of in situ mobilized colloidal particles in packed soil columns. Environ. Sci. Technol. 32(22), 3562-3569.

Ikni, T., Benamar, A., Kadri, M., Ahfir, N.D. and Wang, H.Q. 2013. Particle transport within water-saturated porous media: Effect of pore size on retention kinetics and size selection. C.R. Geosci. 345(9-10), 392-400.

Keating, K. 2014. A laboratory study to determine the effect of surface area and bead diameter on NMR relaxation rates of glass bead packs. Near Surf. Geophys. 12(2), 243-254.

Kretzschmar, R., Barmettler, K., Grolimund, D., Yan, Y.D., Borkovec, M. and Sticher, H. 1997. Experimental determination of colloid deposition rates and collision efficiencies in natural porous media. Water Resour. Res. 33(5), 1129-1137.

Kretzschmar, R. and Sticher, H. 1998. Colloid transport in natural porous media: influence of surface chemistry and flow velocity. Phys. Chem. Earth 23(2), 133-139.

Mao, M., Zheng, X.L., Chen, C., Zhao, K., Yan, C.R., Sharma, P. and Shang, J.Y. 2020. Coupled effect of flow velocity and structural heterogeneity on transport and release of kaolinite colloids in saturated porous media. Environ. Sci. Pollut. Res. 27(28), 35065-35077.

Massei, N., Lacroix, M., Wang, H.Q. and Dupont, J.P. 2002. Transport of particulate material and dissolved tracer in a highly permeable porous medium: comparison of the transfer parameters. J. Contam. Hydrol. 57(1-2), 21-39.

Morales-Chávez, S., Valdez-Grijalva, M.A., Díaz-Viera, M.A., Lucas-Oliveira, E. and Bonagamba, T.J. 2025. A mathematical model of NMR transverse relaxation for pore size distribution estimation in porous media. J. Magn. Reson. 379, 107922.

Nagel, S.M., Strangfeld, C. and Kruschwitz, S. 2021. Application of 1H proton NMR relaxometry to building materials – A review. J. Magn. Reson. Open. 6-7, 100012.

Nishad, S., Al-Raoush, R.I. and Alazaiza, M.Y.D. 2021. Release of colloids in saturated porous media under transient hydro-chemical conditions: A pore-scale study. Colloids and Surfaces A: Physicochemical and Engineering Aspects 614, 126188.

Peng, S., Marone, F. and Dultz, S. 2014. Resolution effect in X-ray microcomputed tomography imaging and small pore's contribution to permeability for a Berea sandstone. J. Hydrol. 510, 403-411.

Samari Kermani, M., Jafari, S., Rahnama, M. and Raoof, A. 2020. Direct pore scale numerical simulation of colloid transport and retention. Part I: Fluid flow velocity, colloid size, and pore structure effects. Adv Water Resour 144, 103694.

Shen, Y., Ueda, T. and Wang, Y. 2025. Multiscale pore structure characterization and permeability analysis based on concrete NMR-CT registration method. Constr. Build. Mater. 493(26), 143287.

Šimůnek, J., Brunetti, G., Jacques, D., van Genuchten, M.T. and Šejna, M. 2024. Developments and applications of the HYDRUS computer software packages since 2016. Vadose Zone J. 23(4), e20310.

Sirivithayapakorn, S. and Keller, A. 2003. Transport of colloids in saturated porous media: A pore-scale observation of the size exclusion effect and colloid acceleration. Water Resour. Res. 39(4), 2002WR001583.

Torkzaban, S., Bradford, S.A., Vanderzalm, J.L., Patterson, B.M., Harris, B. and Prommer, H. 2015. Colloid release and clogging in porous media: Effects of solution ionic strength and flow velocity. J. Contam. Hydrol. 181, 161-171.

Wang, C. 2025. Quantitative analysis of the effect of flow velocity on the size exclusion transport of colloids in saturated porous media. Figshare Dataset.

Wang, C., Duan, Z., Liao, R., Šimůnek, J. and Luo, D. 2025. High-resolution characterization of the size exclusion effect on the transport of low-concentration mixed-size colloids in porous media using a synthetic DNA-labeling method. Environ. Sci. Technol. 59(24), 12232-12243.

Wang, C., Šimůnek, J., Liu, Y., Duan, Z. and Liao, R. 2024. Quantifying the effects of size exclusion on colloidal particle transport in porous media at a pore scale and column scale. Vadose Zone J. 23(6), e20388.

Xiao, D., Lu, S., Lu, Z., Huang, W. and Gu, M. 2016. Combining nuclear magnetic resonance and rate-controlled porosimetry to probe the pore-throat structure of tight sandstones. Pet. Explor. Dev. 43(6), 1049-1059.

Yan, C., Cheng, T. and Shang, J. 2019. Effect of bovine serum albumin on stability and transport of kaolinite colloid. Water Res. 155(15), 204-213.

Zhang, P.Y., Bai, B., Jiang, S.C., Wang, P.C. and Li, H.L. 2016. Transport and deposition of suspended particles in saturated porous media: Effect of hydrodynamic forces and pore structure. Water Supply 16(4), 951-960.

Zhao, W., Zhao, P., Tian, Y., Shen, C., Li, Z., Peng, P. and Jin, C. 2020. Investigation for synergies of ionic strength and flow velocity on colloidal-sized microplastic transport and deposition in porous media using the colloidal-AFM probe. Langmuir 36(22), 6292-6303.

Zhao, Y., Zhu, G., Dong, Y., Danesh, N.N., Chen, Z. and Zhang, T. 2017. Comparison of low-field NMR and microfocus X-ray computed tomography in fractal characterization of pores in artificial cores. Fuel 210(15), 217-226.